induced magnetization in the present field and, second, that it could be a viscous remanent magnetization (VRM) acquired during prolonged exposure of the magnetic minerals to the planetary field and hence reflecting an unknown, but younger, age than that of the smooth plains. Although both of these physical processes are likely to operate, induced magnetizations cannot fully explain the observed HPF field strengths, and the net effect of VRM will be that our estimates of ancient field strength are lower bounds (*10*).

Within the range of uncertainty of crustal thickness (*22*–*24*) and magnetized layer source depths (*10*), most or all of the magnetization could reside within Mercury's crust (Fig. 4). We investigated whether such a scenario is consistent with thermal evolution models, given magnetizations acquired at ~4 Ga. We estimated the depth to T_c for a range of thermal gradients (Fig. 4). The Curie temperature was taken to be 325°C (that of pyrrhotite) as a conservatively low value for our calculations, and we used the maximum average daily surface temperature predicted for a range of Mercury's orbital eccentricities from 0 to 0.4 (*10*, *25*). The results indicate that even for high thermal gradients at 4 Ga (*26*) the depth to T_c in the Suisei Planitia region is at least 20 km. For thermal gradients less than 8 K/km and upper limits on the crustal thickness in the region, the entire crust remains below T_c. These results imply that acquisition and subsequent preservation of an ancient crustal remanence by magnetic carriers with T_c values of at least 325°C are consistent with thermal models (*10*, *26*–*28*), and for carriers with higher T_c some remanence may be carried by upper mantle material. Such a conclusion is predicated on the assumption that the surface temperature pole locations have remained stationary in a body-fixed coordinate system since the time that the remanent magnetization was acquired (*10*). The symmetry of the ancient field with respect to the present rotation axis supports such a presumption by suggesting that, since that epoch, there has been no substantial reorientation of the crust ("true polar wander") with respect to the planet's axis of greatest moment of inertia.

The simplest interpretation of the results presented here is that a core dynamo was present early in Mercury's history. If the dynamo was thermochemically driven [e.g., (*6*, *29*)], this finding provides a strong constraint on models for the thermal evolution of Mercury's interior. In particular, the existence of a core dynamo at the time of smooth plains emplacement presents a new challenge to such models. An early core dynamo can be driven by superadiabatic cooling of the liquid core, but in typical thermal history models this phase has ended by 3.9 Ga. A later dynamo can be driven by the combined effects of cooling and compositional convection associated with formation of a solid inner core (*26*–*28*), but in most thermal history models inner core formation does not start until well after 3.7 Ga. Further progress in understanding the record of Mercury's ancient field can also be made with improved petrological constraints on crustal compositions [e.g., (*30*)], information on the candidate magnetic mineralogies implied, and knowledge of their magnetic properties.

REFERENCES AND NOTES

1. N. F. Ness, K. W. Behannon, R. P. Lepping, Y. C. Whang, K. H. Schatten, *Science* **185**, 151–160 (1974).
2. B. J. Anderson *et al.*, *Science* **321**, 82–85 (2008).
3. B. J. Anderson *et al.*, *Science* **333**, 1859–1862 (2011).
4. B. J. Anderson *et al.*, *J. Geophys. Res.* **117** (E12), E00L12 (2012).
5. C. L. Johnson *et al.*, *J. Geophys. Res.* **117** (E12), E00L14 (2012).
6. H. Cao *et al.*, *Geophys. Res. Lett.* **41**, 4127–4134 (2014).
7. L. C. Philpott *et al.*, *Geophys. Res. Lett.* **41**, 6627–6634 (2014).
8. B. J. Anderson *et al.*, *Geophys. Res. Lett.* **41**, 7444–7452 (2014).
9. H. Korth *et al.*, Modular model for Mercury's magnetospheric magnetic field confined within the average observed magnetopause. JGR Space Physics, doi10.1002/2015JA021022 (2015).
10. Materials and methods are available as supplementary materials on *Science* Online.
11. B. J. Anderson, C. L. Johnson, H. Korth, *Geochem. Geophys. Geosyst.* **14**, 3875–3886 (2013).
12. B. W. Denevi *et al.*, *J. Geophys. Res. Planets* **118**, 891–907 (2013).
13. J. L. Whitten, J. W. Head, B. W. Denevi, S. C. Solomon, *Icarus* **241**, 97–113 (2014).
14. P. K. Byrne *et al.*, *Nat. Geosci.* **7**, 301–307 (2014).
15. S. Marchi *et al.*, *Nature* **499**, 59–61 (2013).
16. M. E. Purucker, J. B. Nicholas, *J. Geophys. Res.* **115** (E12), E12007 (2010).
17. M. A. Wieczorek, B. P. Weiss, S. T. Stewart, *Science* **335**, 1212–1215 (2012).
18. L. R. Nittler *et al.*, *Science* **333**, 1847–1850 (2011).
19. F. M. McCubbin, M. A. Riner, K. E. Vander Kaaden, L. K. Burkemper, *Geophys. Res. Lett.* **39**, L09202 (2012).
20. L. G. Evans *et al.*, *J. Geophys. Res.* **117** (E12), E00L07 (2012).
21. S. Z. Weider, L. R. Nittler, R. D. Starr, T. J. McCoy, S. C. Solomon, *Icarus* **235**, 170–186 (2014).
22. E. Mazarico *et al.*, *J. Geophys. Res. Planets* **119**, 2417–2436 (2014).
23. P. B. James, M. T. Zuber, R. J. Phillips, S. C. Solomon, *J. Geophys. Res. Planets* **120**, 287–310 (2015).
24. S. Padovan, M. A. Wieczorek, J.-L. Margot, N. Tosi, S. C. Solomon, *Geophys. Res. Lett.* **42**, 1029–1038 (2015).
25. A. C. M. Correia, J. Laskar, *Icarus* **201**, 1–11 (2009).
26. J.-P. Williams, O. Aharonson, F. Nimmo, *Geophys. Res. Lett.* **34**, L21201 (2007).
27. M. Grott, D. Breuer, M. Laneuville, *Earth Planet. Sci. Lett.* **307**, 135–146 (2011).
28. N. Tosi, M. Grott, A.-C. Plesa, D. Breuer, *J. Geophys. Res. Planets* **118**, 2474–2487 (2013).
29. S. Stanley, G. A. Glatzmaier, *Space Sci. Rev.* **152**, 617–649 (2010).
30. K. E. Vander Kaaden, F. M. McCubbin, *J. Geophys. Res. Planets* **120**, 195–209 (2015).

ACKNOWLEDGMENTS

We thank the MESSENGER operations and engineering teams for enabling the low-altitude observations reported here. We are also grateful for the contributions of our friend and colleague M. H. Acuña whose expertise was critical to the Magnetometer development. The MESSENGER mission is supported by the NASA Discovery Program and the MESSENGER Participating Scientist Program. C.L.J. and L.C.P. also acknowledge support from the Natural Sciences and Engineering Research Council of Canada. Data from the MESSENGER mission are archived with the NASA Planetary Data System. We thank three reviewers for thoughtful comments that improved the manuscript.

SUPPLEMENTARY MATERIALS

www.sciencemag.org/content/348/6237/892/suppl/DC1
Supplementary Text
Figs. S1 to S11
Tables S1 and S2
References (31–53)

7 February 2015; accepted 28 April 2015
Published online 7 May 2015;
10.1126/science.aaa8720

CARBON CYCLE

The dominant role of semi-arid ecosystems in the trend and variability of the land CO_2 sink

Anders Ahlström,[1,2]* Michael R. Raupach,[3]† Guy Schurgers,[4] Benjamin Smith,[1] Almut Arneth,[5] Martin Jung,[6] Markus Reichstein,[6] Josep G. Canadell,[7] Pierre Friedlingstein,[8] Atul K. Jain,[9] Etsushi Kato,[10] Benjamin Poulter,[11] Stephen Sitch,[12] Benjamin D. Stocker,[13,14] Nicolas Viovy,[15] Ying Ping Wang,[16] Andy Wiltshire,[17] Sönke Zaehle,[6] Ning Zeng[18]

The growth rate of atmospheric carbon dioxide (CO_2) concentrations since industrialization is characterized by large interannual variability, mostly resulting from variability in CO_2 uptake by terrestrial ecosystems (typically termed carbon sink). However, the contributions of regional ecosystems to that variability are not well known. Using an ensemble of ecosystem and land-surface models and an empirical observation-based product of global gross primary production, we show that the mean sink, trend, and interannual variability in CO_2 uptake by terrestrial ecosystems are dominated by distinct biogeographic regions. Whereas the mean sink is dominated by highly productive lands (mainly tropical forests), the trend and interannual variability of the sink are dominated by semi-arid ecosystems whose carbon balance is strongly associated with circulation-driven variations in both precipitation and temperature.

Since the 1960s, terrestrial ecosystems have acted as a substantial sink for atmospheric CO_2, sequestering about one-quarter of anthropogenic emissions in an average year (*1*). This ecosystem service, which helps mitigate climate change by reducing the rate of increase of atmospheric greenhouse gases, is due to an imbalance between the uptake of CO_2 through gross primary production (GPP, the aggregate photosynthesis of plants) and the release of carbon to the atmosphere by ecosystem respiration (R_{eco}) and other losses, including wildfires (C_{fire}). The net carbon flux (net biome production, NBP = GPP − R_{eco} − C_{fire}) results from the small

imbalance between the much larger uptake and release fluxes. Consequently, small fractional variations in either of these fluxes can cause substantial absolute variations in net carbon exchange with the atmosphere. These variations account almost entirely for year-to-year variations around the overall trend in atmospheric concentrations of CO_2 (*2*, *3*).

Modeling studies suggest a large uncertainty of the future magnitude and sign of the carbon sink provided by terrestrial ecosystems (*4*–*8*). Robust projections are crucial to assessments of future atmospheric CO_2 burdens and associated climate change, and are therefore central to the effectiveness of future mitigation policies. Reducing the uncertainty of these projections requires better knowledge of the regions and processes governing the present sink and its variations. Inventories suggest that since the beginning of industrialization, the majority of carbon sequestered by the terrestrial biosphere has accumulated in forest ecosystems of the tropics and temperate zones (*9*). However, the relative contributions of ecosystems of different, climatically distinct, regions to variations in the land sink on interannual to multidecadal time scales are not well characterized. Here, we investigated relative regional contributions to the mean sink, to its trend over recent decades, and to the interannual variability (IAV) around the trend.

We used LPJ-GUESS (*10*–*12*), a biogeochemical dynamic global vegetation model, to simulate the geographic pattern and time course of NBP. LPJ-GUESS explicitly accounts for the dependency of plant production and downstream ecosystem processes on the demography (size structure) and composition of simulated vegetation. We forced the model with historical climate (*13*) and CO_2 concentrations, accounting for emissions from land use change and carbon uptake due to regrowth after agricultural abandonment (*14*). We compared the results to an ensemble of nine ecosystem and land surface model simulations from the TRENDY model intercomparison project (*12*, *15*) (hereinafter TRENDY models; table S1). The TRENDY ensemble is similarly based on historical climate and CO_2 but uses a static 1860 land use mask.

Global NBP, as simulated by LPJ-GUESS, shows strong agreement (r^2 = 0.62) with the Global Carbon Project (GCP) estimate of the net land CO_2 flux—an independent, bookkeeping-based estimate derived as the residual of emissions, atmospheric growth, and ocean uptake of CO_2 (*1*) (Fig. 1A). TRENDY models do not account for land use change. Relative to the GCP land flux estimate, they consequently predict a higher average NBP but similar interannual variation. Moreover, the offset between the TRENDY model ensemble mean and the GCP land flux estimate is comparable to the GCP estimate of mean land use change emission flux for the period 1982–2011 (fLUC).

We divided the global land area into six land cover classes, following the MODIS MCD12C1 land cover classification (*12*, *16*): tropical forests (Fig. 1B), extratropical forest, grasslands and croplands (here combined), semi-arid ecosystems (Fig. 1C), tundra and arctic shrub lands, and sparsely vegetated lands (areas classified as barren) (figs. S1 and S2).

When the global terrestrial CO_2 sink (average NBP) and its trend (1982–2011) are partitioned among land cover classes, we find that tropical forests account for the largest fraction (26%, 0.33 Pg C $year^{-1}$) of the average sink over this period (1.23 Pg C $year^{-1}$) (Fig. 1D). In contrast, we find that semi-arid ecosystems dominate the positive global CO_2 sink trend (57%, 0.04 Pg C $year^{-2}$; global, 0.07 Pg C $year^{-2}$) (Fig. 1E). The TRENDY model ensemble shows a consistent pattern, with

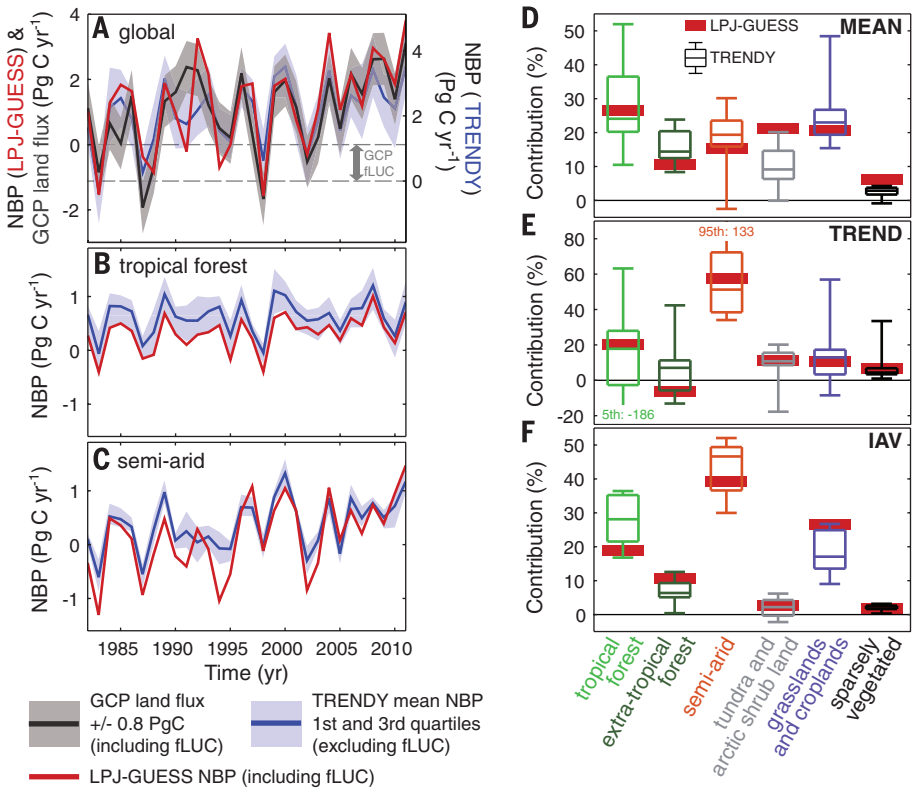

Fig. 1. Global and regional NBP mean, trend, and variations (1982–2011). (**A**) Global NBP from LPJ-GUESS (red line) and GCP land flux time series (black line) with ±0.8 Pg C uncertainty range (shaded gray area). TRENDY models mean (blue line) and first and third quartiles (shaded blue area) are plotted on a separate axis with a time-invariant offset corresponding to the time period average GCP fLUC estimate (1.2 P Pg C $year^{-1}$). (**B**) Tropical forest NBP. LPJ-GUESS (red line) includes emissions from land use change. TRENDY models average (blue line) and first and third quartiles of the ensemble (shaded blue area) do not include emissions from land use change. (**C**) NBP of semi-arid ecosystems from LPJ-GUESS (including land use change emissions) and TRENDY models (excluding land use change emissions); colors and shading as in (B). (**D**) Contribution of land cover classes to global mean NBP (1982–2011) (mean NBP of land cover class as a proportion of mean global NBP). Horizontal lines in box plots show, from top to bottom, 95th, 75th, 50th, 25th, and 5th percentiles. (**E**) Contribution of land cover classes to global NBP trend (land cover class NBP trend as a proportion of global NBP trend). (**F**) Contribution of land cover classes to global NBP IAV (Eq. 1).

[1]Department of Physical Geography and Ecosystem Science, Lund University, 223 62 Lund, Sweden. [2]Department of Earth System Science, School of Earth, Energy and Environmental Sciences, Stanford University, Stanford, CA 94305, USA. [3]Climate Change Institute, Australian National University, Canberra, ACT 0200, Australia. [4]Department of Geosciences and Natural Resource Management, University of Copenhagen, 1350 Copenhagen, Denmark. [5]Institute for Meteorology and Climate Research–Atmospheric Environmental Research, Karlsruhe Institute for Technology, 82476 Garmisch-Partenkirchen, Germany. [6]Biogeochemical Intergration Department, Max Planck Institute for Biogeochemistry, 07745 Jena, Germany. [7]Global Carbon Project, CSIRO Oceans and Atmospheric Flagship, Canberra, ACT, Australia. [8]College of Engineering, Mathematics and Physical Sciences, University of Exeter, Exeter EX4 4QF, UK. [9]Department of Atmospheric Sciences, University of Illinois at Urbana-Champaign, Urbana, IL 61801, USA. [10]Institute of Applied Energy, 105-0003 Tokyo, Japan. [11]Institute on Ecosystems and the Department of Ecology, Montana State University, Bozeman, MT 59717, USA. [12]College of Life and Environmental Sciences, University of Exeter, Exeter EX4 4RJ, UK. [13]Department of Life Sciences, Imperial College, Ascot SL5 7PY, UK. [14]Climate and Environmental Physics, Physics Institute and Oeschger Centre for Climate Change Research, University of Bern, Bern, Switzerland. [15]Laboratoire des sciences du climat et de l'environnement, CEA Saclay, F-91191 Gif-sur-Yvette Cedex, France. [16]CSIRO Ocean and Atmosphere Flagship, PMB 1, Aspendale, Victoria 3195, Australia. [17]Met Office Hadley Centre, Fitzroy Road, Exeter EX1 3PB, UK. [18]Department of Atmospheric and Oceanic Science and Earth System Science Interdisciplinary Center, University of Maryland, College Park, MD 20742, USA.
***Corresponding author. E-mail: anders.ahlstrom@nateko.lu.se**
†Deceased.

tropical forests dominating the mean sink (median 24%) and semi-arid ecosystems dominating the trend (median 51%). The predominance of semi-arid ecosystems in explaining the global land sink trend is consistent with widespread observations of woody encroachment over semi-arid areas (*17*) and increased vegetation greenness inferred from satellite remote sensing over recent decades (*17*–*19*). Likewise, a recent study attributes the majority of the record land sink anomaly of 2011 to the response of semi-arid ecosystems in the Southern Hemisphere, Australia in particular, to an anomalous wet period; the study further postulates a recent increase in the sensitivity of carbon uptake to precipitation for this region, which is attributed to vegetation expansion (*20*).

We further partitioned IAV in global NBP among land cover classes according to the contribution of individual regions (grid cells or land cover classes) to global NBP IAV (*12*). To this end, we adopted an index that scores individual geographic locations according to the consistency, over time, with which the local NBP flux resembles the sign and magnitude of global NBP (fig. S4):

$$f_j = \frac{\sum_t \frac{x_{jt}|X_t|}{X_t}}{\sum_t |X_t|} \quad (1)$$

where x_{jt} is the flux anomaly (departure from a long-term trend) for region j at time t (in years), and X_t is the global flux anomaly, so that $X_t = \sum_j x_{jt}$. By this definition f_j is the average relative anomaly x_{jt}/X_t for region j, weighted with the absolute global anomaly $|X_t|$. Regions receiving higher and positive average scores are inferred to have a larger contribution in governing global NBP IAV, as opposed to regions characterized by smaller or negative (counteracting) scores (fig. S3). The index we adopt does not characterize the variability of ecosystems of different regions, as, for example, the standard deviation would do (fig. S5); rather, it enables a comparison of their relative importance (contribution) in governing global IAV.

Semi-arid ecosystems were found to account for the largest fraction, 39%, of global NBP IAV, exceeding tropical forest (19%), extratropical forest (11%; all forest, 30%), and grasslands and croplands (27%) (Fig. 1F). The TRENDY model ensemble shows a similar partitioning, with semi-arid ecosystems accounting for 47% (median; tropical forests, 28%; extratropical forest, 6%; all forest, 35%). The overall contributions per land cover class are the sum of both positive and negative contributions that result from differences

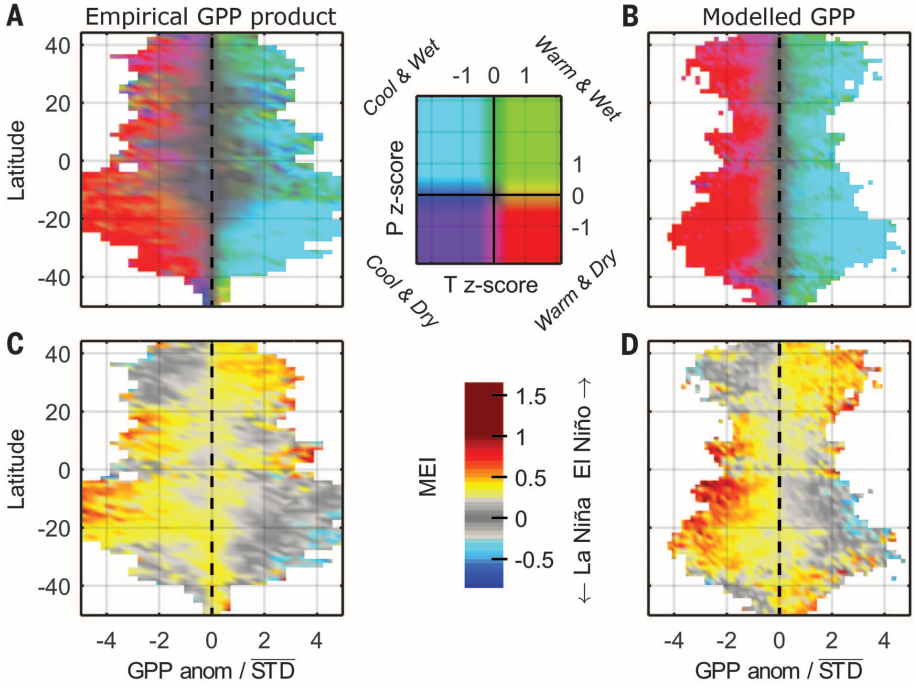

Fig. 2. Climatic covariates of semi-arid ecosystem GPP variations. (**A**) Distribution by latitude of the empirical GPP product anomalies normalized by average standard deviation of GPP in semi-arid lands. The distribution is colored according to average local climatic covariates per latitude zone and distribution bin. (**B**) LPJ-GUESS GPP distribution calculated and colored as in (A). (**C**) Covariation of the multivariate ENSO index [MEI (*31*, *32*)] anomalies with the empirical GPP product. (**D**) Covariation of MEI and modeled GPP anomalies per latitudinal zone. Note that the figure shows the covariates of latitudinal average local GPP anomalies, and not the average covariates based on GPP IAV contribution to NBP IAV.

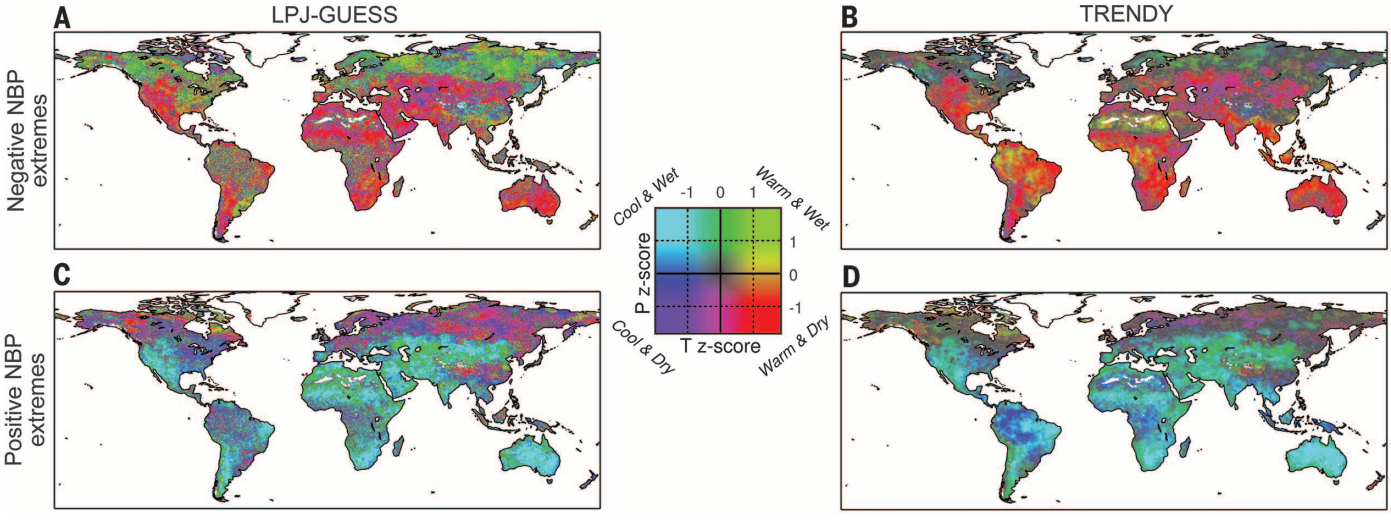

Fig. 3. Climatic covariates of NBP extremes. (**A**) Climatic covariates of LPJ-GUESS negative NBP extremes (1st to 10th percentiles). (**B**) Mean climatic covariates of TRENDY models' negative NBP extremes (1st to 10th percentiles). (**C**) Covariates of LPJ-GUESS positive NBP extremes (90th to 99th percentiles). (**D**) Mean climatic covariates of TRENDY models' positive NBP extremes (90th to 99th percentiles).

in phase between IAV of individual grid cells compared with global IAV (fig. S4). The extent to which negative contributions reduce the overall land cover class contributions is minor for all regions except grasslands and croplands (fig. S6) (LPJ-GUESS, –13%; TRENDY median, –13%) because the latter are distributed widely across climate zones, and because both climate variations and the sensitivity of NBP to climate variations differ among regions.

To partition the global NBP IAV among component fluxes (GPP, R_{eco}, C_{fire}) and among land cover classes, we applied Eq. 1. We found that global NBP IAV is most strongly associated with variation in GPP; interannual GPP anomalies contribute 56% of the global NBP IAV in LPJ-GUESS and a median of 90% in the TRENDY model ensemble. Comparing different land cover classes, the GPP anomalies of semi-arid ecosystems alone contribute 39% in LPJ-GUESS and a median of 65% in the TRENDY model ensemble to global NBP IAV (fig. S7). Semi-arid vegetation productivity thus emerges clearly as the single most important factor governing global NBP IAV.

We used two complementary methods to attribute the variability in GPP—as the inferred primary driver of global NBP IAV—to its environmental drivers. First, we analyzed simulation results from LPJ-GUESS, linking output GPP anomalies to variability in the climatic input data. Second, we used a time-resolved gridded global GPP product derived from upscaled flux tower measurements (*12*, *21*) (hereafter, empirical GPP product). This product uses an empirical upscaling of flux measurements and is thus entirely independent of the modeled GPP in our study.

The three main climatic drivers—temperature (T), precipitation (P), and shortwave radiation (S)—are interdependent and correlated. To account for the combined effects of these drivers, we adopted an analysis of GPP variations from an "impact perspective" (*22*–*24*): We first identified GPP anomalies and then extracted their climatic covariates. The primary challenge of such an analysis on an annual scale is to target climate indices that adequately characterize the "period of climatic influence" (e.g., growing season average, annual averages, minima or maxima of a given climatic forcing). To overcome this challenge, we used semiannual time series of climate drivers constructed via an optimization procedure that weights monthly anomalies of a given climate variable (T, P, or S), accounting for time lags of up to 24 months while making no additional prior assumptions as to the period of influence (*12*). For each GPP event, we extracted climatic covariates as *z* scores of the semiannual climatic drivers.

We evaluated the climatic covariates of GPP anomalies for semi-arid ecosystems from the empirical GPP product and modeled by LPJ-GUESS, focusing on T and P, and found similar responses of GPP to climate with both approaches across all latitude bands (Fig. 2, A and B). Negative GPP anomalies in semi-arid ecosystems are mainly driven by warm and dry (low rainfall) climatic events in most latitudes, suggestive of drought. By contrast, positive GPP anomalies are dominated by cool and wet conditions. Averaging the distributions over latitudes (Fig. 2, A and B) and extracting the climatic covariates per percentile of the GPP distributions shows that GPP varies with climatic conditions on a straight line in T-P space (fig. S8), with a stronger covariation with P than with T. This implies that the full GPP distributions are driven by similar climatic patterns—that is, anomalies that differ in size and sign covary with corresponding differences in size and sign in the drivers. GPP extremes (the tails of the distribution of GPP among years) covary with El Niño–Southern Oscillation (ENSO) across all latitudes (Fig. 2, C and D). In both the model and the empirical GPP product, GPP anomalies are more strongly associated with the positive phase of ENSO (El Niño) than with the negative phase (La Niña); the sign of the relationship varies with latitude. Positive ENSO tends to coincide with negative GPP anomalies in the tropics (30°S to 20°N) and with positive GPP anomalies north of 20°N.

The agreement between climatic covariates of the data-based empirical GPP product and modeled GPP alongside the comparatively robust pattern of the covariation with climate suggests that GPP IAV for semi-arid ecosystems is mediated by climate. Because ENSO covaries with a considerable portion of the GPP distribution, we infer that ENSO is the dominating mode of global circulation variations driving GPP IAV over semi-arid ecosystems. Recent modeling studies have found that extreme El Niño events could become more common under climate change (*25*), which, together with an increased atmospheric demand for water associated with global warming, might exacerbate the impact of El Niño events over semi-arid ecosystems and further increase the role of semi-arid regions in driving global NBP IAV (*26*–*28*).

We repeated the calculation of climatic covariates to simulated NBP for LPJ-GUESS and each of the TRENDY models. The resulting maps of covariates in T-P space are shown as average covariates of negative NBP extremes (Fig. 3, A and B) and positive NBP extremes (Fig. 3, C and D). In general, semi-arid ecosystems stand out as regions in which strong CO_2 uptake events are consistently associated with cool and moist conditions, and strong CO_2 release events with warm and dry conditions. In tropical forests, NBP covaries with both T and P as in semi-arid regions, but also with T alone. In high latitudes, wet or warm and wet conditions lead to negative NBP extremes, whereas dry or warm and dry conditions tend to lead to positive extremes, although the spatial heterogeneity of the covariates is large in this region (Fig. 3).

Our approach offers detailed spatial and temporal disaggregation of drivers and responses, which is important when analyzing drivers or covariates of global NBP IAV because of the high temporal and spatial variability in P (figs. S9 to S11). Using four upscaling levels with increasing spatial and temporal disaggregation [ranging from land surface mean P and T to semiannual P and T, averaged according to the spatial origin of each year's global NBP anomaly (eqs. S5 and S6)], we found that P and NBP IAV become more correlated at higher levels of disaggregation. At the highest disaggregation level, P is almost as strongly correlated with NBP IAV as T, suggesting a strong influence of soil moisture variations on global NBP IAV (*28*). This strong increase in P correlations with disaggregation resolves an apparent conflict between our findings and those of studies using regionally averaged drivers that emphasize the role of T in governing IAV in atmospheric CO_2 (*28*–*30*). For semi-arid ecosystems, T correlations with NBP IAV are slightly stronger than P correlations with NBP IAV (Fig. 4B), partly because of an asymmetric distribution of P and/or an asymmetric response of NBP to P IAV (fig. S12). The correlation of tropical forest P with

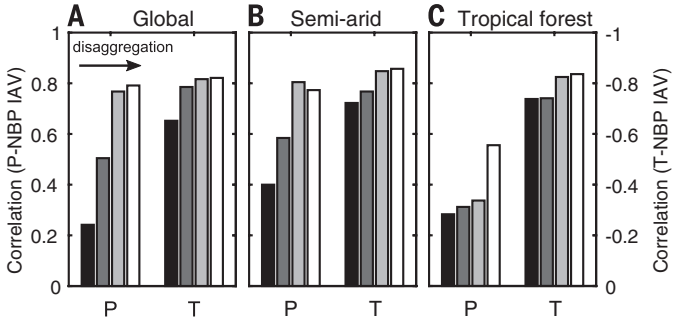

Fig. 4. Correlations between climatic drivers IAV (P and T) and global NBP IAV (mean of all 10 models). (**A**) Global P and T correlations to global NBP IAV. From black to white and left to right, bars represent annual P and T IAV correlations to global NBP IAV with increasing spatial and temporal disaggregation of P and T while averaging to global time series. Black bars represent averaged global land surface P and T weighted by grid cell area; dark gray bars represent P and T weighted by 30-year average contribution to global NBP IAV (Eq. 1 and fig. S4); light gray bars represent averaged P and T weighted by each year's contributions, thus accounting for the difference in the spatial distribution of contributions between years (eqs. S5 and S6); white bars represent semiannual climate drivers averaged to global time series using the annual spatial contributions (as for light gray bars), thereby accounting for the "period of climatic influence" and time lags of up to 24 months. (**B**) Correlations between P and T IAV and global NBP IAV for semi-arid ecosystems. Weights, where applicable, are based on contributions to global NBP IAV as in (A) but with P and T averaged over semi-arid ecosystems only. (**C**) Correlations between P and T IAV and global NBP IAV for tropical forest. Weights, where applicable, are based on contributions to global NBP IAV as in (A) but with P and T averaged over tropical forest only.

NBP IAV increases when we use the semiannual drivers, which suggests the importance of accounting for time lags and the "period of climatic influence" of P variations (*12*), but P correlations with NBP IAV are still weaker than T correlations with NBP IAV (Fig. 4C).

Our analysis provides evidence that semi-arid ecosystems, largely occupying low latitudes, have dominated the IAV and trend of the global land carbon sink over recent decades. Semi-arid regions have been the subject of relatively few targeted studies that place their importance in a global context. Our findings indicate that semi-arid regions and their ecosystems merit increased attention as a key to understanding and predicting interannual to decadal variations in the global carbon cycle.

REFERENCES AND NOTES

1. C. Le Quéré *et al.*, *Earth Syst. Sci. Data* **6**, 235–263 (2014).
2. C. D. Keeling, T. P. Whorf, M. Wahlen, J. van der Plichtt, *Nature* **375**, 666–670 (1995).
3. C. Le Quéré *et al.*, *Nat. Geosci.* **2**, 831–836 (2009).
4. A. Ahlström, G. Schurgers, A. Arneth, B. Smith, *Environ. Res. Lett.* **7**, 044008 (2012).
5. P. Friedlingstein *et al.*, *J. Clim.* **19**, 3337–3353 (2006).
6. A. D. McGuire *et al.*, *Glob. Biogeochem. Cycles* **15**, 183–206 (2001).
7. S. Schaphoff *et al.*, *Clim. Change* **74**, 97–122 (2006).
8. S. Sitch *et al.*, *Glob. Change Biol.* **14**, 2015–2039 (2008).
9. Y. Pan *et al.*, *Science* **333**, 988–993 (2011).
10. A. Ahlström, P. A. Miller, B. Smith, *Geophys. Res. Lett.* **39**, L15403 (2012).
11. B. Smith, I. C. Prentice, M. T. Sykes, *Glob. Ecol. Biogeogr.* **10**, 621–637 (2001).
12. See supplementary materials on *Science* Online.
13. I. Harris, P. D. Jones, T. J. Osborn, D. H. Lister, *Int. J. Climatol.* **34**, 623–642 (2014).
14. G. Hurtt *et al.*, *Clim. Change* **109**, 117–161 (2011).
15. S. Sitch *et al.*, *Biogeosciences* **12**, 653–679 (2015).
16. M. A. Friedl *et al.*, *Remote Sens. Environ.* **114**, 168–182 (2010).
17. N. Andela, Y. Y. Liu, A. I. J. M. van Dijk, R. A. M. de Jeu, T. R. McVicar, *Biogeosciences* **10**, 6657–6676 (2013).
18. R. J. Donohue, T. R. McVicar, M. L. Roderick, *Glob. Change Biol.* **15**, 1025–1039 (2009).
19. R. Fensholt *et al.*, *Remote Sens. Environ.* **121**, 144–158 (2012).
20. B. Poulter *et al.*, *Nature* **509**, 600–603 (2014).
21. M. Jung *et al.*, *J. Geophys. Res.* **16**, G00J07 (2011).
22. J. Zscheischler *et al.*, *Environ. Res. Lett.* **9**, 035001 (2014).
23. M. Reichstein *et al.*, *Nature* **500**, 287–295 (2013).
24. M. D. Smith, *J. Ecol.* **99**, 656–663 (2011).
25. W. Cai *et al.*, *Nat. Clim. Change* **4**, 111–116 (2014).
26. K. E. Trenberth *et al.*, *Nat. Clim. Change* **4**, 17–22 (2014).
27. A. Dai, *Nat. Clim. Change* **3**, 52–58 (2013).
28. X. Wang *et al.*, *Nature* **506**, 212–215 (2014).
29. W. Wang *et al.*, *Proc. Natl. Acad. Sci. U.S.A.* **110**, 13061–13066 (2013).
30. P. M. Cox *et al.*, *Nature* **494**, 341–344 (2013).
31. K. Wolter, M. S. Timlin, in *Proceedings of the 17th Climate Diagnostics Workshop* (University of Oklahoma, Norman, OK, 1993), pp. 52–57; www.esrl.noaa.gov/psd/enso/mei/WT1.pdf.
32. K. Wolter, M. S. Timlin, *Weather* **53**, 315–324 (1998).

ACKNOWLEDGMENTS

This paper is dedicated to the memory of Michael Robin Raupach (1950–2015), whose scientific integrity and novel contributions leave a long-lasting legacy in the field of carbon cycle sciences. The MODIS MOD12C1 land cover product was obtained through the online Data Pool at the NASA Land Processes Distributed Active Archive Center (LP DAAC), USGS/Earth Resources Observation and Science (EROS) Center, Sioux Falls, South Dakota (https://lpdaac.usgs.gov/data_access). Supported by the Royal Physiographic Society in Lund (Birgit and Hellmuth Hertz Foundation), Swedish Research Council grant 637-2014-6895, and the Mistra-SWECIA program (A. Ahlström); EC FP7 grant LUC4C (603542) (A. Arneth); OCE Distinguished Visiting Scientist to the CSIRO Ocean and Atmosphere Flagship, Canberra (B.S.); EC FP7 grant EMBRACE (282672) (A. Arneth, M.R., and B.D.S.); the Australian Climate Change Science Program (J.G.C.); NSF grant AGS 12-43071, U.S. Department of Energy grant DE-SC0006706, and NASA LCLUC program grant NNX14AD94G (A.K.J.); the Environmental Research and Technology Development Fund (S-10) of the Ministry of Environment of Japan (E.K.); CSIRO strategic research funds (Y.P.W.); and NOAA grants NA10OAR4310248 and NA09NES4400006 and NSF grant AGS-1129088 (N.Z.). This study is a contribution to the Lund Centre for Studies of Carbon Cycle and Climate Interactions (LUCCI) and the strategic research areas MERGE and BECC.

SUPPLEMENTARY MATERIALS

www.sciencemag.org/content/348/6237/895/suppl/DC1
Materials and Methods
Figs. S1 to S12
References (*33*–*56*)

26 October 2014; accepted 24 April 2015
10.1126/science.aaa1668

GLACIER MASS LOSS

Dynamic thinning of glaciers on the Southern Antarctic Peninsula

B. Wouters,[1]* A. Martin-Español,[1] V. Helm,[2] T. Flament,[3] J. M. van Wessem,[4] S. R. M. Ligtenberg,[4] M. R. van den Broeke,[4] J. L. Bamber[1]

Growing evidence has demonstrated the importance of ice shelf buttressing on the inland grounded ice, especially if it is resting on bedrock below sea level. Much of the Southern Antarctic Peninsula satisfies this condition and also possesses a bed slope that deepens inland. Such ice sheet geometry is potentially unstable. We use satellite altimetry and gravity observations to show that a major portion of the region has, since 2009, destabilized. Ice mass loss of the marine-terminating glaciers has rapidly accelerated from close to balance in the 2000s to a sustained rate of –56 ± 8 gigatons per year, constituting a major fraction of Antarctica's contribution to rising sea level. The widespread, simultaneous nature of the acceleration, in the absence of a persistent atmospheric forcing, points to an oceanic driving mechanism.

Ice shelves have been identified as sensitive indicators of climate change (*1*). Their retreat along the coast of the Northern Antarctic Peninsula has been noted over recent decades (*2*) and associated with a sudden and prolonged increase in discharge of the inland grounded ice (*3*–*5*), especially for those glaciers overlying deep troughs (*6*). The potential future contribution to sea-level rise of these glaciers relatively modest because their catchments are small compared with those further south (*7*). The Southern Antarctic Peninsula (SAP), including Palmer Land and the Bellinghausen Coast, rests on bedrock below sea level with a retrograde slope (deeper inland) (*8*), which is believed to be an inherently unstable configuration (*9*), permitting rapid grounding line retreat and mass loss to the ocean. Recent modeling results suggest that this marine ice sheet instability may have already been initiated for part of West Antarctica (*10*, *11*).

The SAP is home to a number of fast flowing, marine terminating glaciers, many of which are still unnamed. Laser [ICESat, 2003–2009 (*12*)] and radar [Envisat, 2003– 2010 (*13*)] altimetry identified moderate surface-lowering concentrated within a narrow strip along the coast, in particular near the grounding line of the Ferrigno Ice Stream (*14*), contrasted by widespread thickening further inland. Observations from the Gravity Recovery and Climate Experiment (GRACE) mission show that these opposing signals compensated each other, resulting in a near-zero mass balance for 2002–2010 (*15*).

The Cryosat-2 satellite, launched in April 2010, provides elevation measurements of land and sea ice at a high spatial resolution up to a latitude of 88°. In contrast to conventional altimetry missions such as Envisat, Cryosat-2's dual antenna and Doppler processing results in improved resolution and geolocation of the elevation measurement (*16*). Because of the long satellite repeat period of 369 days, it has a dense track spacing in our region of interest, which is a major advantage compared with the roughly 10-times-coarser ICESat track spacing. Two recent studies using Cryosat-2 data observed thinning along the coast of the Bellinghausen Sea (*17*, *18*). Such elevation changes may result from either a decrease in surface mass balance (SMB) (accumulation minus ablation), compaction of the firn column, or an increase in the ice flow speed (also termed dynamic thinning). Both studies attributed the surface-lowering to interannual changes in SMB, based on the strong accumulation variability observed in the Gomez ice core (70.36°W, 73.59°S) (*18*, *19*). Here, we take SMB and firn compaction into account and show that the

[1]Bristol Glaciology Centre, University of Bristol, Bristol, UK. [2]Alfred-Wegener-Institut Helmholtz-Zentrum für Polar- und Meeresforschung, Bremerhaven, Germany. [3]Laboratoire d'Etudes en Géophysique et Océanographie Spatiales, Toulouse, France. [4]Institute for Marine and Atmospheric Research, Utrecht University, Netherlands.
*Corresponding author. E-mail: bert.wouters@bristol.ac.uk

www.sciencemag.org/content/348/6237/895/suppl/DC1

Supplementary Materials for

The dominant role of semi-arid ecosystems in the trend and variability of the land CO_2 sink

Anders Ahlström,* Michael R. Raupach, Guy Schurgers, Benjamin Smith, Almut Arneth, Martin Jung, Markus Reichstein, Josep G. Canadell, Pierre Friedlingstein, Atul K. Jain, Etsushi Kato, Benjamin Poulter, Stephen Sitch, Benjamin D. Stocker, Nicolas Viovy, Ying Ping Wang, Andy Wiltshire, Sönke Zaehle, Ning Zeng

*Corresponding author. E-mail: anders.ahlstrom@nateko.lu.se

Published 22 May 2015, *Science* **348**, 895 (2015)
DOI: 10.1126/science.aaa1668

This PDF file includes:

Materials and Methods

Figs. S1 to S12

References

Materials and Methods

LPJ-GUESS simulations

The dynamic global vegetation model (DGVM) LPJ-GUESS (*10*, *11*) was forced by climate from CRU TS3.21 (*13*) and time-variant information on land use (*14*). LPJ-GUESS is a second-generation DGVM in which vegetation dynamics result from growth and competition for light, space and soil resources among woody plant individuals and a herbaceous understory in each of a number (100 in this study) of replicate patches in each grid cell. The patches account for the distribution within a landscape representative of the grid cell as a whole of vegetation stands with different histories of disturbance and stand development (succession). Disturbances are implemented as stochastic events with an expected frequency of 0.01 yr^{-1} at patch level. In addition, wildfires are simulated prognostically based on fuel (litter) load, dryness and physical conditions (*33*). GPP, autotrophic and heterotrophic respiration, carbon allocation and phenology, canopy gas exchange, soil hydrology and organic matter dynamics follow the approach of LPJ-DGVM (*34*, *35*). Plant functional type (PFT) settings were as described in (*10*).

TRENDY-models

The ensemble of TRENDY-model results is a combination of results prepared for the global carbon budget of 2013 (*1*) and 2014 (*36*) through the TRENDY project, where the latest available version has been used. We use the S2 simulations where a time invariant pre-industrial land use mask (*14*) was applied (year 1860). The TRENDY model results presented here thus represent carbon cycle responses of the biophysical land surface to climate and CO_2 change, omitting emissions due to land use change or regrowth. Simulations are forced with climate information from CRU-NCEP (*37*).The ensemble consists of results from nine ecosystem models and land surface models (Table S1).

Table S1. TRENDY models.

Model name	Carbon budget year	Spatial resolution (longitude x latitude)	Land surface model	Dynamic vegetation	Disturbance types	Source
CABLE	2014	0.5° x 0.5°	yes	no	-	(*38*, *39*)
ISAM	2014	0.5° x 0.5°	yes	yes	-	(*40-42*)
JULES	2014	1.875° x ~1.6°	yes	yes	-	(*43*)
LPJ	2013	0.5° x 0.5°	no	yes	fire	(*35*, *44*)
LPX-Bern	2014	1° x 1°	no	yes	fire	(*45*)
ORCHIDEE	2013	0.5°x 0.5°	yes	yes	crop harvest	(*46*)
O-CN	2013	1° x 1.2°	yes	no	-	(*47*, *48*)
VEGAS	2014	0.5° x 0.5°	yes	yes	fire	(*49*, *50*)
VISIT	2014	0.5° x 0.5°	no	no	fire, erosion	(*51*, *52*)

Empirical GPP product

The empirical GPP product originates from upscaled FLUXNET eddy-covariance tower measurements (*21*). The overall upscaling procedure involves three main steps: (I) processing and quality control of the FLUXNET data, (II) training a machine learning based regression algorithm (Model Tree Ensembles, MTEs (*53*)) for tower observed monthly GPP using site-level explanatory variables and satellite observed fraction of absorbed photosynthetic active radiation, and (III) applying the established MTEs for global upscaling, using gridded data sets of the same explanatory variables. 25 individual model trees were forced for each biosphere-atmosphere flux using gridded monthly inputs from 1982 to 2011. The best estimate of a biosphere-atmosphere flux for further analysis is the median over the 25 estimates for each pixel and month.

Half-hourly FLUXNET eddy covariance measurements were processed using standardized procedures of gap filling and quality control (*54*, *55*), and the data were subsequently aggregated into monthly means. 29 explanatory variables of four types were used to train the model tree ensemble to predict biosphere-atmosphere fluxes globally (see also Table 1 in *21*), including (I) monthly fAPAR from the SeaWiFS sensor, precipitation, and temperature (both in situ measured); (II) annual changes of the fAPAR that describe properties of vegetation structure such as minimum, maximum, mean, and amplitude; (III) mean annual climate such as mean annual temperature, precipitation, sunshine hours, relative humidity, potential evapotranspiration, climatic water balance (precipitation–potential evaporation), and their seasonal dynamics; and (IV) the vegetation type according to the IGBP classification plus a flag regarding the photosynthetic pathway (C3, C4, C3/C4) (in situ information).

Land cover classes

We defined six land cover classes together covering the global land area, tropical forest, extra-tropical forest (boreal and temperate), semi-arid ecosystems, tundra and arctic shrub land, grasslands and land under agriculture (crops, here combined), and areas classified as barren (sparsely vegetated).

The global land surface was first divided into three main classes, forest, savanna and shrub lands, and grass lands and crop lands. This classification is based on a MODIS land cover classification (MCD12C1, type3) from satellite borne remote sensing (*17*), remapped using a majority filter to a spatial resolution of 0.5x0.5°. The MODIS forest category was split to tropical and extra-tropical forest using the Köppen-Geiger climate classification system (*56*). Tropical forest are defined by the Köppen-Geiger A climate group, where mean temperature of all months over the study period (1982-2011) do not fall below 18°C. Savanna and shrub lands were divided at a natural break at latitude 45°N into semi-dry ecosystems (latitudes < 45°N) and tundra and arctic shrub lands (latitudes > 45°N).

Partitioning of interannual variations

Partitioning of IAV to regions or grid cells follow the definition of Equation S1. For a given flux (NBP or GPP, R_{eco} and C_{fire}), the contribution of the IAV of a grid cell or land cover class *j* to the global NBP IAV is defined as:

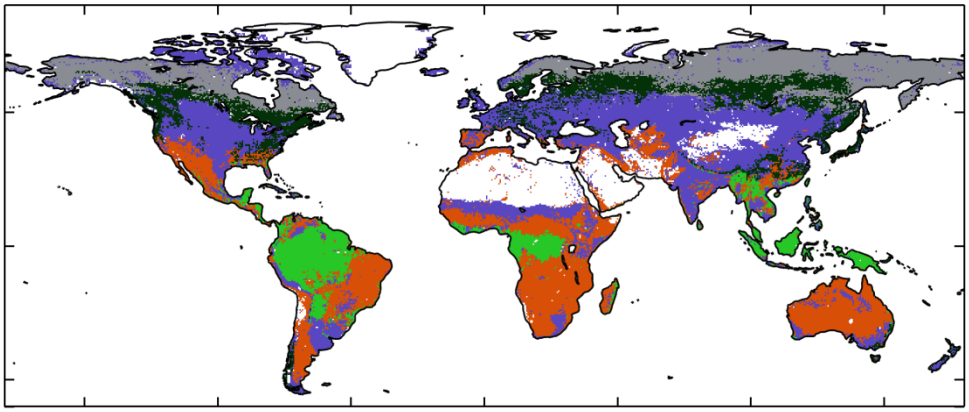

Fig. S1. Map of land cover classes. Tropical forests are shown in light green, extra-tropical forest in dark green, semi-arid ecosystems in orange, tundra and arctic shrub land in grey, grasslands and crops in blue, sparsely vegetated regions in white.

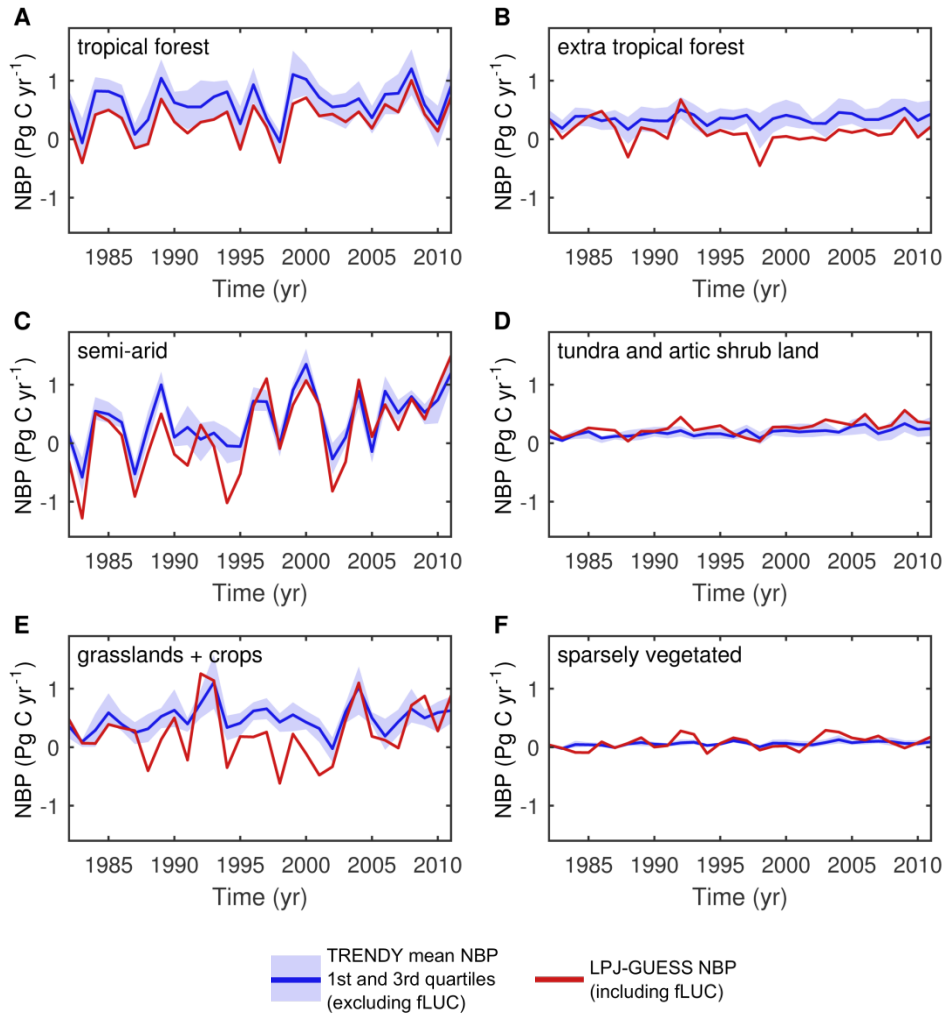

Fig. S2. NBP time-series of land cover classes from LPJ-GUESS and TRENDY-models. LPJ-GUESS accounts for emissions associated with land use change and the TRENDY-model results do not, explaining part of the difference between the two datasets. (A) NBP from LPJ-GUESS over tropical forest (red line), TRENDY-ensemble mean NBP (blue line) and 25th to 75th percentile (1st and 3rd quartiles) NBP (light blue shading). (B) Extra-tropical forest. (C) Semi-arid ecosystems. (D) Tundra and arctic shrub land. (E) Grasslands + crops. (F) Sparsely vegetated.

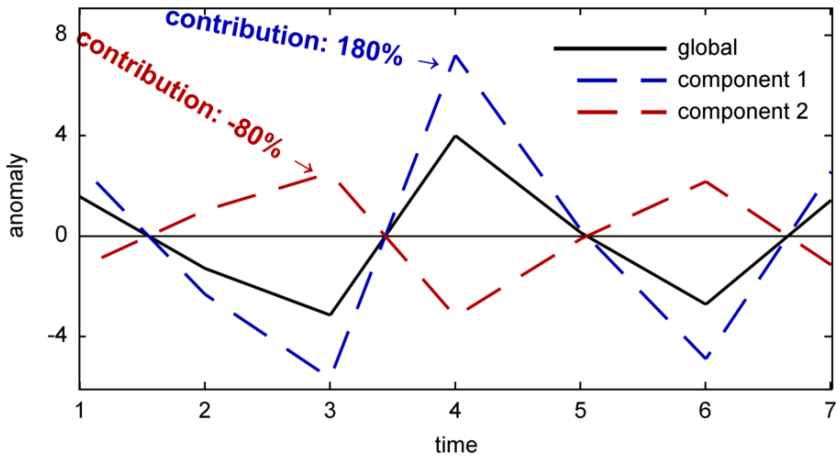

Fig. S3. Illustration of application of Equation S1. The black solid line represent a global signal and the blue and the red lines represent two components that sum to the global signal. Since component 1 varies in phase with the global signal with larger anomalies its contribution is larger than 100%, in this example, 180%. Component 2 on the other hand varies with smaller amplitude and with an opposite phase, and, since it together with component 1 sums to the global signal it must have a contribution of -80%, which would also be the result of Equation S1. Component 2 is in this example therefore dampening the global variations that would arise from only component 1.

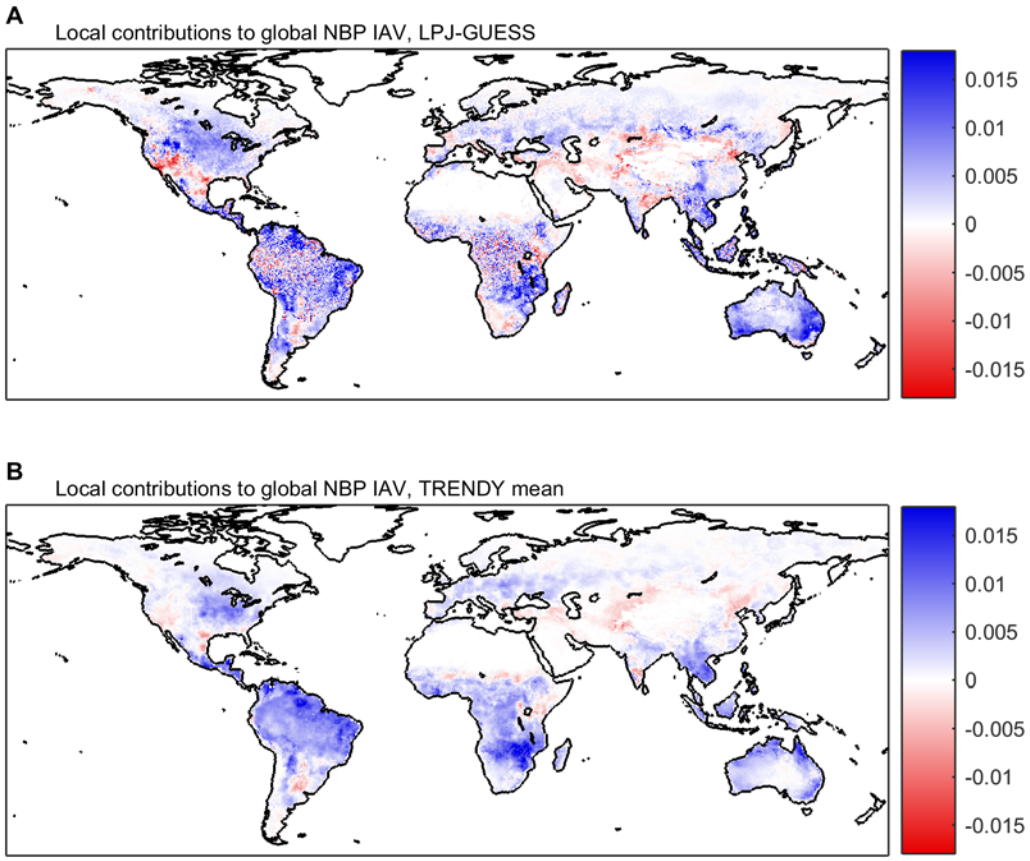

Fig. S4. Local NBP contributions to global NBP interannual variations. (A) Local NBP contributions to global NBP IAV as simulated by LPJ-GUESS (%). (B) Local NBP contributions to global NBP IAV, mean of TRENDY models (%).

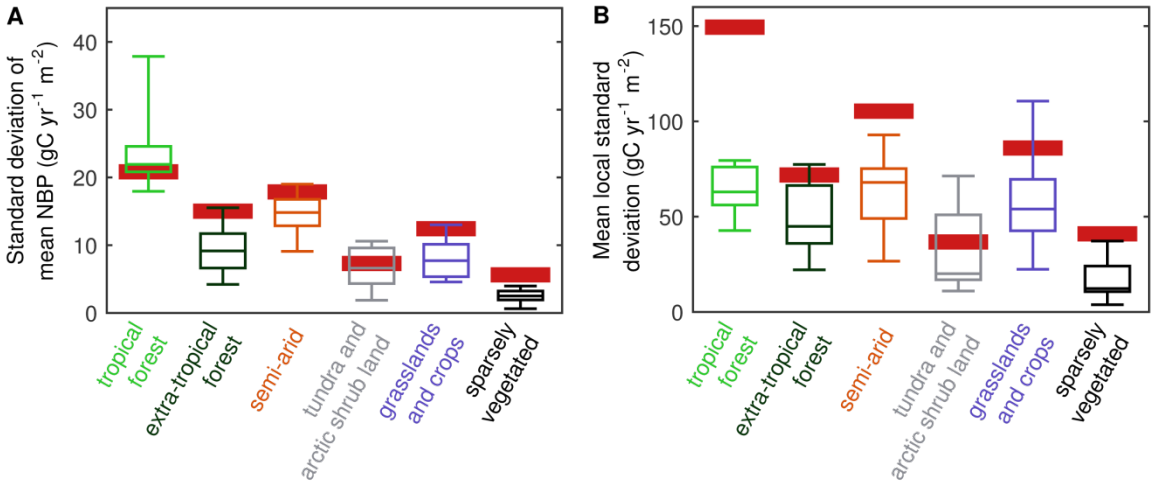

Fig. S5. Standard deviations (sd) of NBP IAV over land cover classes. (A) calculated on aggregated local NBP per land cover class; and (B) calculated for each grid cell and averaged for each land cover class. Legend as in Figure 1 (D-F). LPJ-GUESS shows higher variation among grid cells compared with TRENDY model ensemble owing mainly to stochastic representations of vegetation dynamic processes including mortality and disturbances. LPJ-GUESS sd is comparable to other models in (A) because effects of stochastic disturbances cancel between grid cells, while effects of among-grid variability are conserved in (B).
NB: the figures show local standard deviations per area unit (m^{-2}) and not contributions to global IAV. Because the variations are presented per area unit, differences in total extent between the land cover classes are not accounted for in these figures.

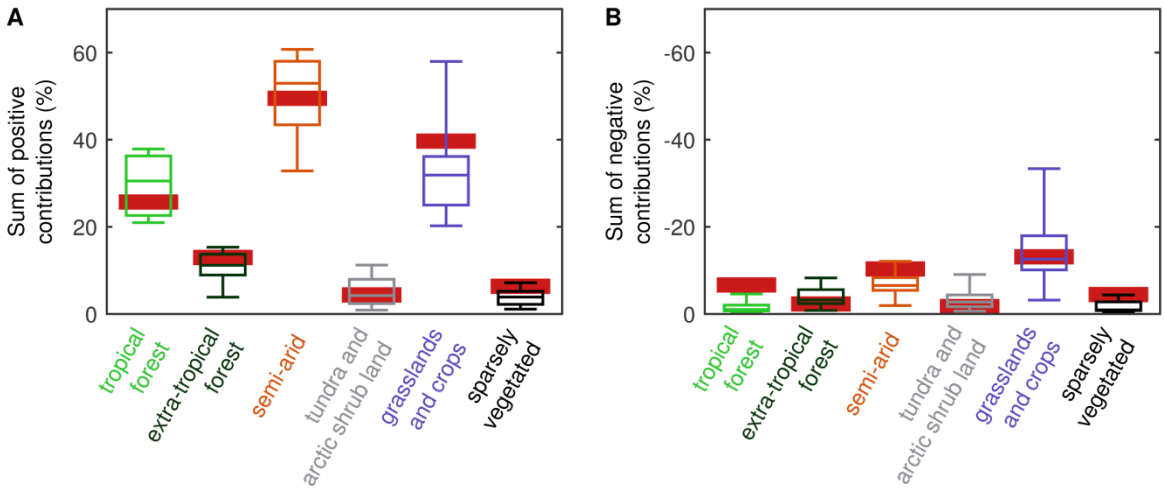

Fig. S6. Regional positive and negative NBP contributions to global NBP IAV. Panels A and B sum to the overall contribution to global NBP IAVs presented in Figure 1C. Legend as in Figure 1 (D-F). (A) Sum of positive only regional contributions to global NBP IAVs. (B) Sum of negative only regional contributions to global NBP IAV. The two panels illustrate how the contribution per land cover class could change by assessing a subset of a land cover class, e.g. dividing extra tropical forest into temperate and boreal forest. Since the overall contribution of a land cover class is the sum of local contributions, the maximum contribution of a subset of a land cover class, if all negatively contributing grid cells are removed, are shown in panel A. The relatively large negative contribution of grasslands and crops is likely due to the distribution of the land cover class across climate zones globally resulting in differences in climate variations and sensitivities to climate variations between locations.

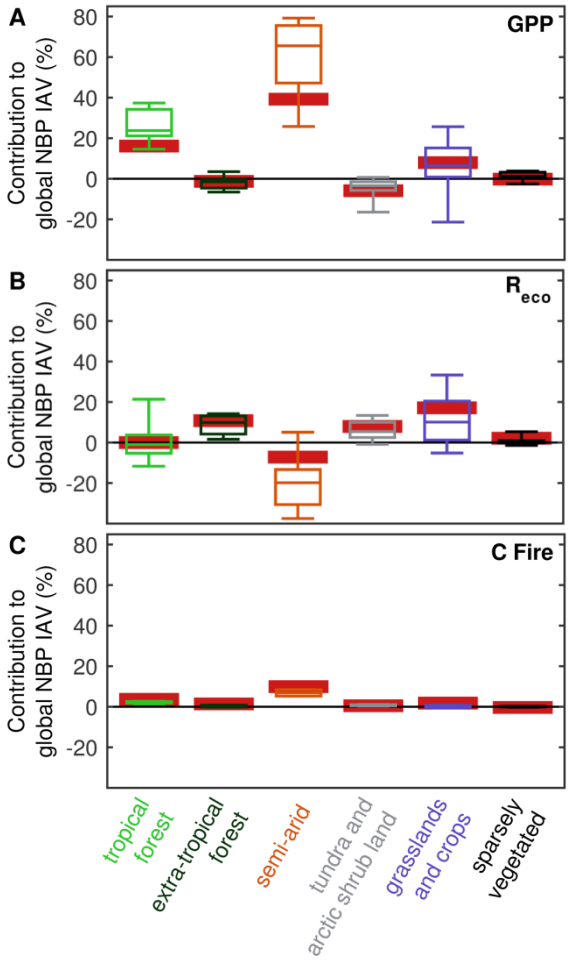

Fig. S7. Regional NBP component contributions to global NBP IAV. Legend as in Figure 1 (D-F). (A) Regional GPP contributions to global NBP IAV. (B) Regional ecosystem respiration (autotrophic + heterotrophic respiration) contributions to global NBP IAV. Decomposition of biomass residues originating from land use change is included in the LPJ-GUESS R_{eco}. (C) Regional wildfire emission (Cfire) contributions to global NBP IAV.

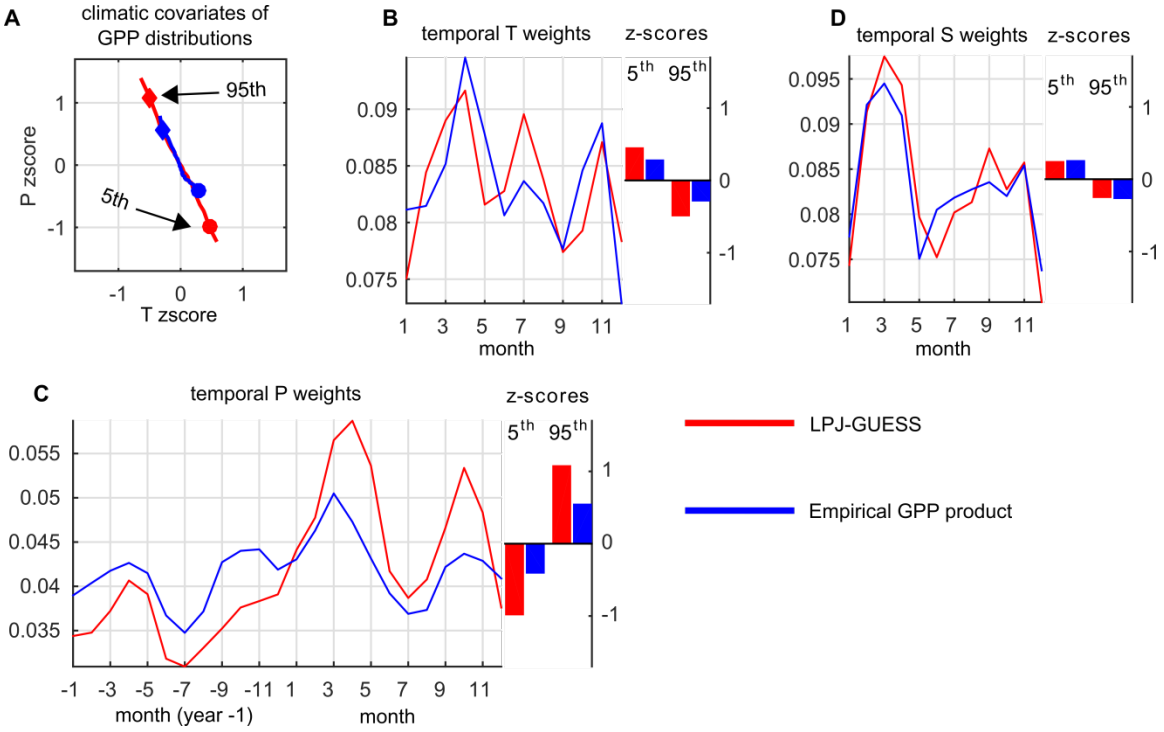

Fig. S8. Climatic covariates and temporal loadings of semi-arid ecosystems. (A) Climatic T-P space covariates of GPP percentiles 1-99 averaged over all semi-arid land weighted by grid cell area. Circles indicate the climatic covariates of the 5th percentile and diamonds indicate the 95th percentile covariates. The similar slope of the empirical GPP product and modelled GPP indicates that variations in both datasets covary with similar variations in T and P. The full distribution of both GPP datasets covary stronger with P than T; indicated by a general slope inclining towards the vertical P axis; over all percentiles of the GPP distributions, the corresponding P standardized anomaly is about twice that of the standardized T anomaly. (B) Lines indicate the monthly weights of monthly T IAV influence on GPP IAV. Bars represent the average T covariates for the 5th and 95th percentiles. (C) Lines indicate the monthly weights of monthly P IAV influence on GPP IAV. Bars represent the average P covariates for the 5th and 9th percentiles. (D) Lines indicate the monthly weights of the monthly downward shortwave radiation (S) IAV influence on GPP IAV. Bars represent the average S covariates for the 5th and 9th percentiles.

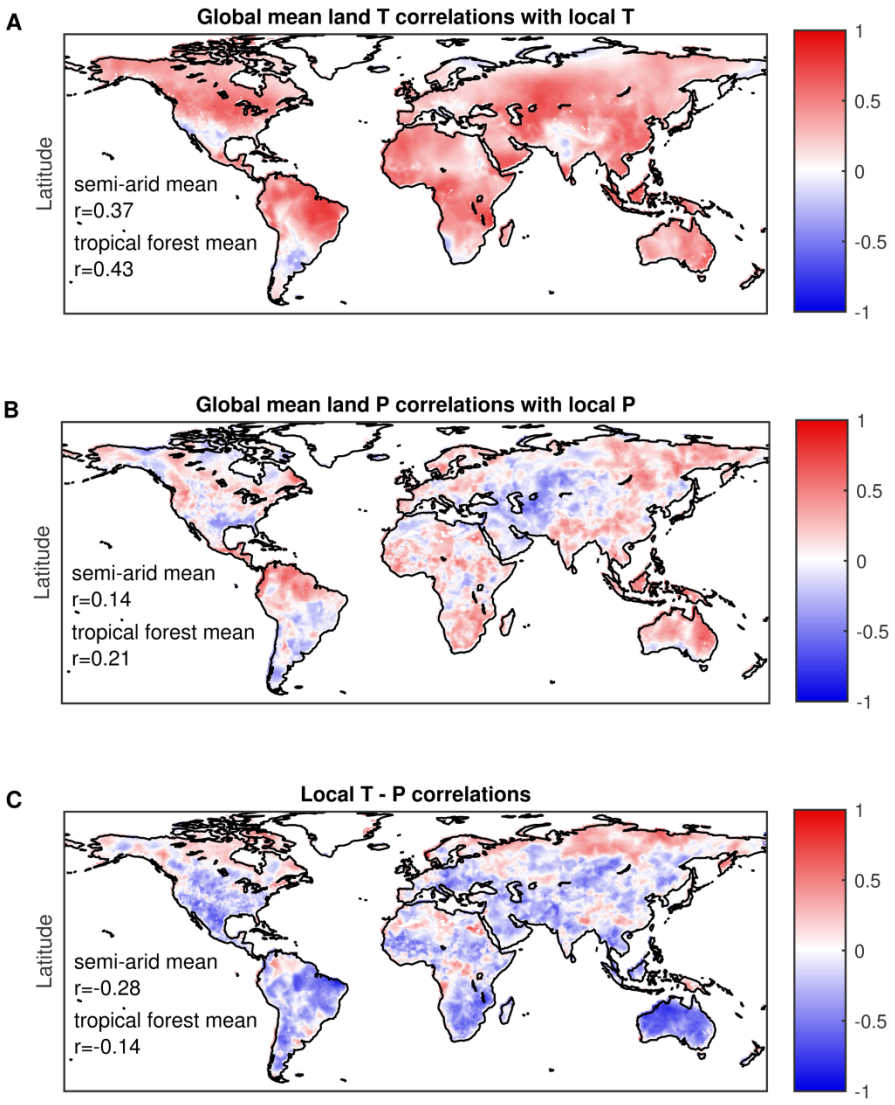

Fig. S9. Spatial properties of interannual variations of temperature and precipitation. (A) Correlations between global mean land surface temperature and local temperature interannual variations. (B) Correlations between global mean land surface precipitation and local precipitation interannual variations. (C) Local correlations between temperature and precipitation interannual variations.

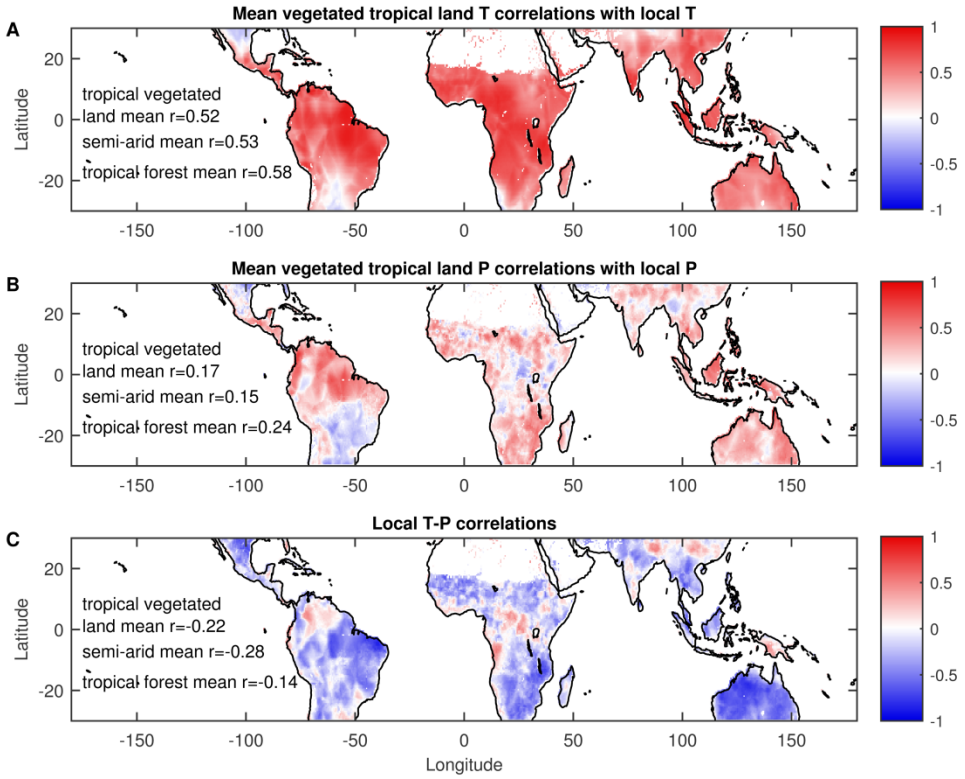

Fig. S10. Spatial properties of interannual variations of temperature and precipitation over tropical vegetated land. (A) Correlations between mean tropical vegetated land surface temperature and local temperature interannual variations. (B) Correlations between mean tropical vegetated land surface precipitation and local precipitation interannual variations. (C) Local correlations between temperature and precipitation interannual variations.

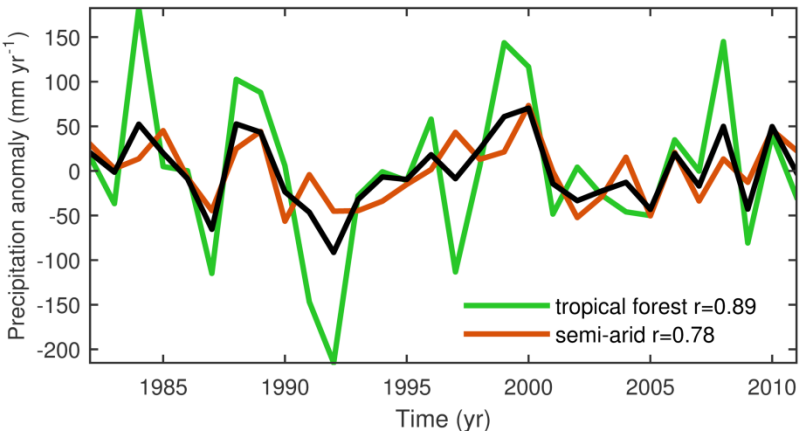

Fig. S11. Correlations between mean tropical vegetated land precipitation (black line) and tropical forest and semi-arid ecosystem interannual variations. The figure illustrates how an averaged climate signal can be affected by a region with large variations. In this example precipitation anomalies are larger over tropical forest than semi-arid ecosystems, leading to a domination of tropical forest precipitation in the aggregated time series.

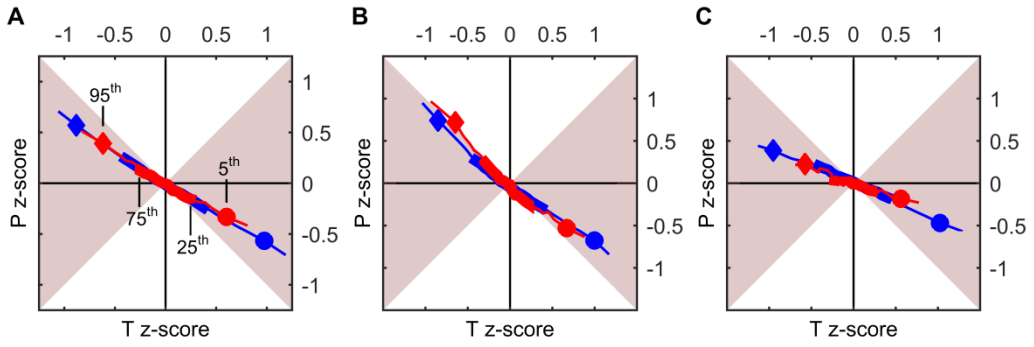

Fig. S12. Climatic covariates of contribution weighted average NBP IAV distributions. (A) Climatic covariates of global NBP IAV, spatially weighted by 30-year average contributions to global NBP IAV (Eq S1, Fig S4). LPJ-GUESS is shown in red and TRENDY-models average in blue. Shaded area illustrates where NBP covaries more with T than P, and white where NBP covaries more with P than T. (B) Climatic covariates of semi-arid ecosystems NBP IAV, spatially weighted by 30-year average contributions to global NBP IAV. Positive anomalies (percentiles >50) covaries more with P than negative anomalies due to an asymmetry in the P distribution (positive P anomalies > -negative P anomalies), and/or an asymmetrical response of NBP to P. (C) Climatic covariates of tropical forest NBP IAV, spatially weighted by 30-year average contributions to global NBP IAV.
NB: The figures show the average climatic (semi-annual) covariates of NBP IAV weighted by average contributions over 1982-2011, and is therefore not fully comparable to the correlations presented in Figure 4 at the highest level of disaggregation, where the global P and T time series are based on the spatial contributions of each year. In contrast to the correlations however, the percentile-covariation distributions shown in here are not sensitive to the non-normal distribution of P (as in (B)).

References

1. C. Le Quéré, G. P. Peters, R. J. Andres, R. M. Andrew, T. A. Boden, P. Ciais, P. Friedlingstein, R. A. Houghton, G. Marland, R. Moriarty, S. Sitch, P. Tans, A. Arneth, A. Arvanitis, D. C. E. Bakker, L. Bopp, J. G. Canadell, L. P. Chini, S. C. Doney, A. Harper, I. Harris, J. I. House, A. K. Jain, S. D. Jones, E. Kato, R. F. Keeling, K. Klein Goldewijk, A. Körtzinger, C. Koven, N. Lefèvre, F. Maignan, A. Omar, T. Ono, G.-H. Park, B. Pfeil, B. Poulter, M. R. Raupach, P. Regnier, C. Rödenbeck, S. Saito, J. Schwinger, J. Segschneider, B. D. Stocker, T. Takahashi, B. Tilbrook, S. van Heuven, N. Viovy, R. Wanninkhof, A. Wiltshire, S. Zaehle, Global carbon budget 2013. *Earth Syst. Sci. Data* **6**, 235–263 (2014). doi:10.5194/essd-6-235-2014

2. C. D. Keeling, T. P. Whorf, M. Wahlen, J. van der Plichtt, Interannual extremes in the rate of rise of atmospheric carbon dioxide since 1980. *Nature* **375**, 666–670 (1995). doi:10.1038/375666a0

3. C. Le Quéré, M. R. Raupach, J. G. Canadell, G. Marland et al, C. Le Quéré et al, C. Le Quéré et al, M. R. Raupach, J. G. Canadell, G. Marland, L. Bopp, P. Ciais, T. J. Conway, S. C. Doney, R. A. Feely, P. Foster, P. Friedlingstein, K. Gurney, R. A. Houghton, J. I. House, C. Huntingford, P. E. Levy, M. R. Lomas, J. Majkut, N. Metzl, J. P. Ometto, G. P. Peters, I. C. Prentice, J. T. Randerson, S. W. Running, J. L. Sarmiento, U. Schuster, S. Sitch, T. Takahashi, N. Viovy, G. R. van der Werf, F. I. Woodward, Trends in the sources and sinks of carbon dioxide. *Nat. Geosci.* **2**, 831–836 (2009). doi:10.1038/ngeo689

4. A. Ahlström, G. Schurgers, A. Arneth, B. Smith, Robustness and uncertainty in terrestrial ecosystem carbon response to CMIP5 climate change projections. *Environ. Res. Lett.* **7**, 044008 (2012). doi:10.1088/1748-9326/7/4/044008

5. P. Friedlingstein, P. Cox, R. Betts, L. Bopp, W. von Bloh, V. Brovkin, P. Cadule, S. Doney, M. Eby, I. Fung, G. Bala, J. John, C. Jones, F. Joos, T. Kato, M. Kawamiya, W. Knorr, K. Lindsay, H. D. Matthews, T. Raddatz, P. Rayner, C. Reick, E. Roeckner, K.-G. Schnitzler, R. Schnur, K. Strassmann, A. J. Weaver, C. Yoshikawa, N. Zeng, Climate–carbon cycle feedback analysis: Results from the C4MIP model intercomparison. *J. Clim.* **19**, 3337–3353 (2006). doi:10.1175/JCLI3800.1

6. A. D. McGuire, S. Sitch, J. S. Clein, R. Dargaville, G. Esser, J. Foley, M. Heimann, F. Joos, J. Kaplan, D. W. Kicklighter, R. A. Meier, J. M. Melillo, B. Moore III, I. C. Prentice, N. Ramankutty, T. Reichenau, A. Schloss, H. Tian, L. J. Williams, U. Wittenberg, Carbon balance of the terrestrial biosphere in the twentieth century: Analyses of CO_2, climate and land use effects with four process-based ecosystem models. *Glob. Biogeochem. Cycles* **15**, 183–206 (2001). doi:10.1029/2000GB001298

7. S. Schaphoff, W. Lucht, D. Gerten, S. Sitch, W. Cramer, I. C. Prentice, Terrestrial biosphere carbon storage under alternative climate projections. *Clim. Change* **74**, 97–122 (2006). doi:10.1007/s10584-005-9002-5

8. S. Sitch, C. Huntingford, N. Gedney, P. E. Levy, M. Lomas, S. L. Piao, R. Betts, P. Ciais, P. Cox, P. Friedlingstein, C. D. Jones, I. C. Prentice, F. I. Woodward, Evaluation of the terrestrial carbon cycle, future plant geography and climate-carbon cycle feedbacks using five Dynamic Global Vegetation Models (DGVMs). *Glob. Change Biol.* **14**, 2015–2039 (2008). doi:10.1111/j.1365-2486.2008.01626.x

9. Y. Pan, R. A. Birdsey, J. Fang, R. Houghton, P. E. Kauppi, W. A. Kurz, O. L. Phillips, A. Shvidenko, S. L. Lewis, J. G. Canadell, P. Ciais, R. B. Jackson, S. W. Pacala, A. D. McGuire, S. Piao, A. Rautiainen, S. Sitch, D. Hayes, A large and persistent carbon sink in the world's forests. *Science* **333**, 988–993 (2011). Medline doi:10.1126/science.1201609

10. A. Ahlström, P. A. Miller, B. Smith, Too early to infer a global NPP decline since 2000. *Geophys. Res. Lett.* **39**, L15403 (2012). doi:10.1029/2012GL052336

11. B. Smith, I. C. Prentice, M. T. Sykes, Representation of vegetation dynamics in the modelling of terrestrial ecosystems: Comparing two contrasting approaches within European climate space. *Glob. Ecol. Biogeogr.* **10**, 621–637 (2001). doi:10.1046/j.1466-822X.2001.00256.x

12. See supplementary materials on *Science* Online.

13. I. Harris, P. D. Jones, T. J. Osborn, D. H. Lister, Updated high-resolution grids of monthly climatic observations—the CRU TS3.10 dataset. *Int. J. Climatol.* **34**, 623–642 (2014). doi:10.1002/joc.3711

14. G. Hurtt, L. P. Chini, S. Frolking, R. A. Betts, J. Feddema, G. Fischer, J. P. Fisk, K. Hibbard, R. A. Houghton, A. Janetos, C. D. Jones, G. Kindermann, T. Kinoshita, K. Klein Goldewijk, K. Riahi, E. Shevliakova, S. Smith, E. Stehfest, A. Thomson, P. Thornton, D. P. van Vuuren, Y. P. Wang, Harmonization of land-use scenarios for the period 1500–2100: 600 years of global gridded annual land-use transitions, wood harvest, and resulting secondary lands. *Clim. Change* **109**, 117–161 (2011). doi:10.1007/s10584-011-0153-2

15. S. Sitch, P. Friedlingstein, N. Gruber, S. D. Jones, G. Murray-Tortarolo, A. Ahlström, S. C. Doney, H. Graven, C. Heinze, C. Huntingford, S. Levis, P. E. Levy, M. Lomas, B. Poulter, N. Viovy, S. Zaehle, N. Zeng, A. Arneth, G. Bonan, L. Bopp, J. G. Canadell, F. Chevallier, P. Ciais, R. Ellis, M. Gloor, P. Peylin, S. L. Piao, C. Le Quéré, B. Smith, Z. Zhu, R. Myneni, Recent trends and drivers of regional sources and sinks of carbon dioxide. *Biogeosciences* **12**, 653–679 (2015). doi:10.5194/bg-12-653-2015

16. M. A. Friedl, D. Sulla-Menashe, B. Tan, A. Schneider, N. Ramankutty, A. Sibley, X. Huang, MODIS Collection 5 global land cover: Algorithm refinements and characterization of new datasets. *Remote Sens. Environ.* **114**, 168–182 (2010). doi:10.1016/j.rse.2009.08.016

17. N. Andela, Y. Y. Liu, A. I. J. M. van Dijk, R. A. M. de Jeu, T. R. McVicar, Global changes in dryland vegetation dynamics (1988–2008) assessed by satellite remote sensing: Comparing a new passive microwave vegetation density record with reflective greenness data. *Biogeosciences* **10**, 6657–6676 (2013). doi:10.5194/bg-10-6657-2013

18. R. J. Donohue, T. R. McVicar, M. L. Roderick, Climate-related trends in Australian vegetation cover as inferred from satellite observations, 1981–2006. *Glob. Change Biol.* **15**, 1025–1039 (2009). doi:10.1111/j.1365-2486.2008.01746.x

19. R. Fensholt, T. Langanke, K. Rasmussen, A. Reenberg, S. D. Prince, C. Tucker, R. J. Scholes, Q. B. Le, A. Bondeau, R. Eastman, H. Epstein, A. E. Gaughan, U. Hellden, C. Mbow, L. Olsson, J. Paruelo, C. Schweitzer, J. Seaquist, K. Wessels, Greenness in semi-arid areas across the globe 1981–2007—an Earth Observing Satellite based analysis of trends and drivers. *Remote Sens. Environ.* **121**, 144–158 (2012). doi:10.1016/j.rse.2012.01.017

20. B. Poulter, D. Frank, P. Ciais, R. B. Myneni, N. Andela, J. Bi, G. Broquet, J. G. Canadell, F. Chevallier, Y. Y. Liu, S. W. Running, S. Sitch, G. R. van der Werf, Contribution of semi-arid ecosystems to interannual variability of the global carbon cycle. *Nature* **509**, 600–603 (2014). Medline doi:10.1038/nature13376

21. M. Jung, M. Reichstein, H. A. Margolis, A. Cescatti, A. D. Richardson, M. A. Arain, A. Arneth, C. Bernhofer, D. Bonal, J. Chen, D. Gianelle, N. Gobron, G. Kiely, W. Kutsch, G. Lasslop, B. E. Law, A. Lindroth, L. Merbold, L. Montagnani, E. J. Moors, D. Papale, M. Sottocornola, F. Vaccari, C. Williams, Global patterns of land-atmosphere fluxes of carbon dioxide, latent heat, and sensible heat derived from eddy covariance, satellite, and meteorological observations. *J. Geophys. Res.* **16**, G00J07 (2011). doi:10.1029/2010JG001566

22. J. Zscheischler, M. D. Mahecha, J. von Buttlar, S. Harmeling, M. Jung, A. Rammig, J. T. Randerson, B. Schölkopf, S. I. Seneviratne, E. Tomelleri, S. Zaehle, M. Reichstein, A few extreme events dominate global interannual variability in gross primary production. *Environ. Res. Lett.* **9**, 035001 (2014). doi:10.1088/1748-9326/9/3/035001

23. M. Reichstein, M. Bahn, P. Ciais, D. Frank, M. D. Mahecha, S. I. Seneviratne, J. Zscheischler, C. Beer, N. Buchmann, D. C. Frank, D. Papale, A. Rammig, P. Smith, K. Thonicke, M. van der Velde, S. Vicca, A. Walz, M. Wattenbach, Climate extremes and the carbon cycle. *Nature* **500**, 287–295 (2013). Medline doi:10.1038/nature12350

24. M. D. Smith, An ecological perspective on extreme climatic events: A synthetic definition and framework to guide future research. *J. Ecol.* **99**, 656–663 (2011). doi:10.1111/j.1365-2745.2011.01798.x

25. W. Cai, S. Borlace, M. Lengaigne, P. van Rensch, M. Collins, G. Vecchi, A. Timmermann, A. Santoso, M. J. McPhaden, L. Wu, M. H. England, G. Wang, E. Guilyardi, F.-F. Jin, Increasing frequency of extreme El Nino events due to greenhouse warming. *Nat. Clim. Change* **4**, 111–116 (2014). doi:10.1038/nclimate2100

26. K. E. Trenberth, A. Dai, G. van der Schrier, P. D. Jones, J. Barichivich, K. R. Briffa, J. Sheffield, Global warming and changes in drought. *Nat. Clim. Change* **4**, 17–22 (2014). doi:10.1038/nclimate2067

27. A. Dai, Increasing drought under global warming in observations and models. *Nat. Clim. Change* **3**, 52–58 (2013). doi:10.1038/nclimate1633

28. X. Wang, S. Piao, P. Ciais, P. Friedlingstein, R. B. Myneni, P. Cox, M. Heimann, J. Miller, S. Peng, T. Wang, H. Yang, A. Chen, A two-fold increase of carbon cycle sensitivity to tropical temperature variations. *Nature* **506**, 212–215 (2014). Medline doi:10.1038/nature12915

29. W. Wang, P. Ciais, R. R. Nemani, J. G. Canadell, S. Piao, S. Sitch, M. A. White, H. Hashimoto, C. Milesi, R. B. Myneni, Variations in atmospheric CO_2 growth rates coupled with tropical temperature. *Proc. Natl. Acad. Sci. U.S.A.* **110**, 13061–13066 (2013). Medline doi:10.1073/pnas.1219683110

30. P. M. Cox, D. Pearson, B. B. Booth, P. Friedlingstein, C. Huntingford, C. D. Jones, C. M. Luke, Sensitivity of tropical carbon to climate change constrained by carbon dioxide variability. *Nature* **494**, 341–344 (2013). Medline doi:10.1038/nature11882

31. K. Wolter, M. S. Timlin, in *Proceedings of the 17th Climate Diagnostics Workshop* (University of Oklahoma, Norman, OK, 1993), pp. 52–57; www.esrl.noaa.gov/psd/enso/mei/WT1.pdf.

32. K. Wolter, M. S. Timlin, Measuring the strength of ENSO events: How does 1997/98 rank? *Weather* **53**, 315–324 (1998). doi:10.1002/j.1477-8696.1998.tb06408.x

33. K. Thonicke, S. Venevsky, S. Sitch, W. Cramer, The role of fire disturbance for global vegetation dynamics: Coupling fire into a Dynamic Global Vegetation Model. *Glob. Ecol. Biogeogr.* **10**, 661–677 (2001). doi:10.1046/j.1466-822X.2001.00175.x

34. D. Gerten, S. Schaphoff, U. Haberlandt, W. Lucht, S. Sitch, Terrestrial vegetation and water balance–hydrological evaluation of a dynamic global vegetation model. *J. Hydrol.* **286**, 249–270 (2004). doi:10.1016/j.jhydrol.2003.09.029

35. S. Sitch, B. Smith, I. C. Prentice, A. Arneth, A. Bondeau, W. Cramer, J. O. Kaplan, S. Levis, W. Lucht, M. T. Sykes, K. Thonicke, S. Venevsky, Evaluation of ecosystem dynamics, plant geography and terrestrial carbon cycling in the LPJ dynamic global vegetation model. *Glob. Change Biol.* **9**, 161–185 (2003). doi:10.1046/j.1365-2486.2003.00569.x

36. C. Le Quéré, R. Moriarty, R. M. Andrew, G. P. Peters, P. Ciais, P. Friedlingstein, S. D. Jones, S. Sitch, P. Tans, A. Arneth, T. A. Boden, L. Bopp, Y. Bozec, J. G. Canadell, F. Chevallier, C. E. Cosca, I. Harris, M. Hoppema, R. A. Houghton, J. I. House, A. Jain, T. Johannessen, E. Kato, R. F. Keeling, V. Kitidis, K. Klein Goldewijk, C. Koven, C. S. Landa, P. Landschützer, A. Lenton, I. D. Lima, G. Marland, J. T. Mathis, N. Metzl, Y. Nojiri, A. Olsen, T. Ono, W. Peters, B. Pfeil, B. Poulter, M. R. Raupach, P. Regnier, C. Rödenbeck, S. Saito, J. E. Salisbury, U. Schuster, J. Schwinger, R. Séférian, J. Segschneider, T. Steinhoff, B. D. Stocker, A. J. Sutton, T. Takahashi, B. Tilbrook, G. R. van der Werf, N. Viovy, Y.-P. Wang, R. Wanninkhof, A. Wiltshire, N. Zeng, Global carbon budget 2014. *Earth Syst. Sci. Data Discuss.* **7**, 521–610 (2014). doi:10.5194/essdd-7-521-2014

37. Y. Wei, S. Liu, D. N. Huntzinger, A. M. Michalak, N. Viovy, W. M. Post, C. R. Schwalm, K. Schaefer, A. R. Jacobson, C. Lu, H. Tian, D. M. Ricciuto, R. B. Cook, J. Mao, X. Shi, The North American Carbon Program Multi-scale Synthesis and Terrestrial Model Intercomparison Project—Part 2: Environmental driver data. *Geosci. Model Dev.* **7**, 2875–2893 (2014). doi:10.5194/gmd-7-2875-2014

38. Y. P. Wang, E. Kowalczyk, R. Leuning, G. Abramowitz, M. R. Raupach, B. Pak, E. van Gorsel, A. Luhar, Diagnosing errors in a land surface model (CABLE) in the time and frequency domains. *J. Geophys. Res.* **116**, G01034 (2011). doi:10.1029/2010JG001385

39. Y. P. Wang, R. M. Law, B. Pak, A global model of carbon, nitrogen and phosphorus cycles for the terrestrial biosphere. *Biogeosciences* **7**, 2261–2282 (2010). doi:10.5194/bg-7-2261-2010

40. R. Barman, A. K. Jain, M. Liang, Climate-driven uncertainties in modeling terrestrial gross primary production: A site level to global-scale analysis. *Glob. Change Biol.* **20**, 1394–1411 (2014). Medline doi:10.1111/gcb.12474

41. B. El-Masri, R. Barman, P. Meiyappan, Y. Song, M. Liang, A. K. Jain, Carbon dynamics in the Amazonian Basin: Integration of eddy covariance and ecophysiological data with a land surface model. *Agric. For. Meteorol.* **182–183**, 156–167 (2013). doi:10.1016/j.agrformet.2013.03.011

42. A. K. Jain, P. Meiyappan, Y. Song, J. I. House, CO_2 emissions from land-use change affected more by nitrogen cycle, than by the choice of land-cover data. *Glob. Change Biol.* **19**, 2893–2906 (2013). Medline doi:10.1111/gcb.12207

43. D. B. Clark, L. M. Mercado, S. Sitch, C. D. Jones, N. Gedney, M. J. Best, M. Pryor, G. G. Rooney, R. L. H. Essery, E. Blyth, O. Boucher, R. J. Harding, C. Huntingford, P. M. Cox, The Joint UK Land Environment Simulator (JULES), model description—Part 2: Carbon fluxes and vegetation dynamics. *Geosci. Model Dev.* **4**, 701–722 (2011). doi:10.5194/gmd-4-701-2011

44. B. Poulter, D. C. Frank, E. L. Hodson, N. E. Zimmermann, Impacts of land cover and climate data selection on understanding terrestrial carbon dynamics and the CO_2 airborne fraction. *Biogeosciences* **8**, 2027–2036 (2011). doi:10.5194/bg-8-2027-2011

45. B. D. Stocker, R. Roth, F. Joos, R. Spahni, M. Steinacher, S. Zaehle, L. Bouwman, Xu-Ri, I. C. Prentice, Multiple greenhouse-gas feedbacks from the land biosphere under future climate change scenarios. *Nat. Clim. Change* **3**, 666–672 (2013). doi:10.1038/nclimate1864

46. G. Krinner, N. Viovy, N. de Noblet-Ducoudré, J. Ogée, J. Polcher, P. Friedlingstein, P. Ciais, S. Sitch, I. C. Prentice, A dynamic global vegetation model for studies of the coupled atmosphere-biosphere system. *Glob. Biogeochem. Cycles* **19**, GB1015 (2005). doi:10.1029/2003GB002199

47. S. Zaehle, P. Ciais, A. D. Friend, V. Prieur, Carbon benefits of anthropogenic reactive nitrogen offset by nitrous oxide emissions. *Nat. Geosci.* **4**, 601–605 (2011). doi:10.1038/ngeo1207

48. S. Zaehle, A. D. Friend, Carbon and nitrogen cycle dynamics in the O-CN land surface model: 1. Model description, site-scale evaluation, and sensitivity to parameter estimates. *Glob. Biogeochem. Cycles* **24**, GB1005 (2010). doi:10.1029/2009GB003521

49. N. Zeng, Glacial-interglacial atmospheric CO_2 change—The glacial burial hypothesis. *Adv. Atmos. Sci.* **20**, 677–693 (2003). doi:10.1007/BF02915395

50. N. Zeng, A. Mariotti, P. Wetzel, Terrestrial mechanisms of interannual CO_2 variability. *Glob. Biogeochem. Cycles* **19**, GB1016 (2005). doi:10.1029/2004GB002273

51. A. Ito, M. Inatomi, Use of a process-based model for assessing the methane budgets of global terrestrial ecosystems and evaluation of uncertainty. *Biogeosciences* **9**, 759–773 (2012). doi:10.5194/bg-9-759-2012

52. E. Kato, T. Kinoshita, A. Ito, M. Kawamiya, Y. Yamagata, Evaluation of spatially explicit emission scenario of land-use change and biomass burning using a process-based biogeochemical model. *J. Land Use Sci.* **8**, 104–122 (2013). doi:10.1080/1747423X.2011.628705

53. M. Jung, M. Reichstein, A. Bondeau, Towards global empirical upscaling of FLUXNET eddy covariance observations: Validation of a model tree ensemble approach using a biosphere model. *Biogeosciences* **6**, 2001–2013 (2009). doi:10.5194/bg-6-2001-2009

54. A. J. Moffat, D. Papale, M. Reichstein, D. Y. Hollinger, A. D. Richardson, A. G. Barr, C. Beckstein, B. H. Braswell, G. Churkina, A. R. Desai, E. Falge, J. H. Gove, M. Heimann, D. Hui, A. J. Jarvis, J. Kattge, A. Noormets, V. J. Stauch, Comprehensive comparison of gap-filling techniques for eddy covariance net carbon fluxes. *Agric. For. Meteorol.* **147**, 209–232 (2007). doi:10.1016/j.agrformet.2007.08.011

55. D. Papale, M. Reichstein, M. Aubinet, E. Canfora, C. Bernhofer, W. Kutsch, B. Longdoz, S. Rambal, R. Valentini, T. Vesala, D. Yakir, Towards a standardized processing of Net Ecosystem Exchange measured with eddy covariance technique: Algorithms and uncertainty estimation. *Biogeosciences* **3**, 571–583 (2006). doi:10.5194/bg-3-571-2006

56. W. Köppen, in *Handbuch der Klimatologie*, W. Köppen, R. Geiger, Eds. (Gebrüder Borntraeger, Berlin, 1936).